Nanoscale Advances

ROYAL SOCIETY OF CHEMISTRY

PAPER

View Article Online
View Journal | View Issue

Cite this: *Nanoscale Adv.*, 2025, **7**, 7003

Hierarchically porous RhB-encapsulated ZIF-7 as a dual-emission fluorescence probe for ultrasensitive detection of melamine in infant formulations

Sreevidhya K. B. [ab] and Suvardhan Kanchi [*ab]

Received 28th June 2025
Accepted 9th September 2025

DOI: 10.1039/d5na00633c

rsc.li/nanoscale-advances

Melamine is an unauthorized food additive and a highly concerning adulterant in foods that can occur either accidently or intentionally in dairy products, with potential health risks upon exposure to higher concentrations. An ultrasensitive fluorescent probe based on dual emissive RhB_x@ZIF-7 was developed to detect melamine. In this study, a fluorescent dye, Rhodamine B (RhB), was successfully encapsulated into the metal–organic framework (MOF) pores of ZIF-7 to form a fluorescent probe (RhB_{30}@ZIF-7), with dual emission properties to enable the detection of melamine at low concentrations. RhB_{30}@ZIF-7 was optimized by varying experimental parameters, including temperature (25 °C), pH (7.0), incubation time (10 min), and probe concentration (1 mg mL^{-1}), to enhance its sensitivity and selectivity. The observed fluorescent quenching towards melamine was primarily attributed to the mechanisms of the internal filtering effect (IFE), due to absorption of the excitation wavelength by melamine, causing a turn-off response in the system. The limit of detection (LOD) and limit of quantification (LOQ) were found to be 0.47 μM and 1.4 μM, respectively, with an R^2 of 0.99. This study reveals the previously unexplored enhanced fluorescence of RhB_{30}@ZIF-7 and elucidates the contribution of the intermolecular interaction between RhB and ZIF-7 to fluorescence sensing, paving the way for food safety monitoring.

1. Introduction

Melamine (2,4,6-triamino-1,3,5-triazine) is an industrially attractive compound that is extensively used in the molding of plastics with formaldehyde; in the manufacturing of cookware, plastic crockery as well as adhesives; and as a fertilizer additive.[1,2] It is also utilized as a pharmaceutical drug carrier. The high nitrogen content in melamine (66% nitrogen by mass) leads to its illegal usage in the food industry, as it imparts properties of protein to the food composition. Thus, melamine is profoundly adulterated in dairy products, infant formulations, milk, livestock feed, and a range of protein-rich diets by unethical manufacturers to falsely inflate the protein level to an unusual amount owing to its low cost and ability to mimic analytical protein characteristics in standard Kjeldahl and Dumas tests.[3–5] The adulteration of food products using harmful chemicals/substances can pose an elevated risk to consumer health, necessitating the efficient and continuous monitoring of toxins and chemicals in food matrices. Melamine has not been authorized as a food additive by the Codex Alimentarius Commission (CAC) and national authorities and is listed as a hazard if inhaled, ingested, or absorbed through the skin.[6] Chronic exposure to melamine can cause cancer or kidney damage.[2] The World Health Organization (WHO)'s International Agency for Research on Cancer placed melamine on the list of 2B carcinogens in 2012 because of its ability to harm human health.[6] The US Food and Drug Administration (FDA) recommended the maximum allowable limits of 2.5 mg kg^{-1} and 1 mg kg^{-1} for melamine in adult food and infant formulations, respectively.[2] Intake of more than the permitted amount of melamine can lead to the development of insoluble crystals of melamine cyanurate in the kidneys, tissue damage, as well as acute kidney failure in humans and animals, which is potentially fatal.[7,8] Melamine in high concentrations can cause food poisoning, especially in children and infants; therefore, the WHO has established a tolerable daily intake (TDI) of 0.2 mg kg^{-1} of body weight per day for humans based on CAC.[9] The severe health implications of melamine adulteration across all age groups and animals necessitate the development of a selective and sensitive sensor for detection in dairy products and food.

To date, several approaches have been used to analyze melamine, including high performance liquid chromatography (HPLC),[10] liquid chromatography/tandem mass spectrometry (LC/MS),[11] gas chromatography-mass spectrometry (GC-MS),[12,13] electrophoresis,[14] immune assay analysis (ELISA – Enzyme-

[a]*Department of Chemistry, CHRIST University, Bengaluru 560029, India. E-mail: suvardhan.k@christuniversity.in*

[b]*Centre for Renewable Energy and Environmental Sustainability, CHRIST University, Bengaluru 560 029, India*

Linked Immunosorbent Assay),[15,16] surface-enhanced Raman spectroscopy (SERS)[17] and electrochemical sensing.[18,19] Despite the selectivity and sensitivity of these methods, their practical implementation in regular analysis is limited by costly equipment, complex sample pretreatment, skilled manpower, complicated operation, and the use of chemical solvents.[20] Over the past decade, sensor technologies have been increasingly recognized as supplements to traditional instrumentation analysis for the detection of contaminants/adulterants in dairy products.[21–23] Optical sensors are often rapid, efficient, cost-effective, user-friendly, and sensitive to a certain extent for the detection of adulterants in a wide range of complex matrices.[24] However, the developed probe's sensitivity and selectivity remain challenging. Therefore, to address sensitivity and selectivity, it is highly essential to develop new probes using mesoporous self-assembly structures. Among these, metal–organic frameworks (MOFs) are being progressively investigated owing to their potential for detecting chemical contaminants in food products, including dairy products. Metal organic frameworks (MOFs) are hybrid crystals consisting of an inorganic framework and organic building blocks. Furthermore, advancements have been made in improving the physicochemical properties of MOF-based sensors by post-synthetic modifications, such as doping, encapsulation, surface functionalization, and defect engineering.[25] Luminescent metal organic frameworks have recently attracted significant attention due to their structural and chemical benefits, including high surface area, luminescent modes, and quick response time.[26]

A dual emission fluorescent platform was developed for the sensing and quantification of melamine in milk powder over a wide range of concentrations using Tb@NH_2-MIL-253 (Al) MOF as a fluorescent probe with a low LOD of 40 nM.[20] Similarly, a nanocomposite of Ag-MOFs doped with a magnetic nanocatalyst for sensing melamine with simple visualization showed an LOD of 1.8 ppm with a recovery of 77%.[27] In another study, both Hg^+ and melamine were detected using CeO_2-incorporated MIL(Fe) *via* colorimetric detection. The CeO_2-MIL(Fe) composite showed peroxidase-like activity for melamine and achieved LODs of 8 nM.[28] The nano-ceria encapsulated MOF, CeO_2@NH_2-MIL(Fe)-based fluorescent biosensor, was reported for the detection of melamine and Pb^{2+} with LODs of 7.6 nM and 1.3 nM, respectively, using a hybridization chain reaction amplification strategy.[29] A method in which ZIF-8 was confined with highly luminescent perovskite quantum dots ($CsPbBr_3$) using a two-step *in situ* growth method to detect Cu^{2+} and melamine showed LODs of 2.64 nM and 4.66 nM, respectively. This sensor exhibited an "on–off–on" mechanism by implementing the quenching property of Cu^{2+} on $CsPbBr_3$/HZIF-8, which was then restored by competitive adsorption by the amine group in melamine.[30] The Zr-based MOF was reported to be a ratiometric fluorescent probe for sensing melamine, with an LOD of 90 nM. UiO-66 was encapsulated in tris(2,2-bipyridyl)ruthenium(II)chloride hexahydrate ($[Ru(bpy)_3]^{2+}$) using a solvothermal method to achieve a dual-emission fluorescent probe.[31] MOFs encapsulated with metals, nanoparticles, and dyes have been studied for the detection of melamine, while the combination of RhB_{30}@ZIF-7 has not been explored.

MOFs with zeolitic architectures, also known as zeolitic imidazolate frameworks (ZIFs), a subfamily of MOFs, are one of the significant research areas due to their combination of properties from both MOFs and zeolites.[32] ZIFs have zeolite framework topologies with transition metals occupying tetrahedral positions and imidazolate units as bridging ones, resulting in a high surface area, micro porosity, and superior chemical and thermal stability.[33,34] Most ZIFs exhibit inherent luminescence either by virtue of the metal nodes or the organic ligands that link them together, featuring only a single emission with low stability and sensitivity. However, fluorescence as a result of incorporated guest molecules significantly contributes to highly efficient fluorescence-based sensing.[35] ZIF-7 is a well-known candidate in the ZIF family of MOFs with two porous pockets in a single porous capsular shell, which was discovered by Huang *et al.* in 2003.[36] When integrated with fluorescent molecules, their unique luminescent properties are enhanced, thereby gaining traction in the field of optical sensing.[23] Inherent luminescence combined with a fluorescent guest molecule can form a dual emission system with improved luminescence performance.[37–41]

In the current study, a guest@MOF approach utilizes the porous nature of MOFs as a 'host' to confine fluorescent molecules as 'guest' within the extended MOF structures for optical sensing applications.[42,43] Dyes are ideal guests for use in guest@MOF systems,[44] as most dyes do not emit fluorescence in the solid state due to aggregation-caused quenching (ACQ).[45,46] Dye monomers separated *via* encapsulation into MOF pores can induce fluorescence while existing in the solid state and are durable over time.[47–50] Rhodamine-B (RhB) is a cationic dye with high PLQY and stability.[51] RhB is included in MOFs, such as ZIF-71,[52] Zr-MOF,[53] ZIF-8,[4] Co MOF,[54] ZIF-7 III Metal organic nanosheets,[55] Zn MOF,[56] and Eu(BTC),[57] for the detection of cations, nitro explosives, pesticides, extraction of different phenols, detection of phenolic compounds in food, volatile organic compounds, or picric acid.

Rhodamine-B was chosen as the guest molecule for the ZIF-7 framework due to its structural compatibility. It is a planar molecule in which the Ph-COOH moiety is perpendicular to the molecular plane of the xanthane backbone. Thus, it is favourable for encapsulation within the pockets of host ZIF-7. A careful investigation of the host structure revealed a pocket of 17.34 × 11.47 Å with an entry of 6.31 × 4.79 Å. The dimensions of guest species (16.19 × 12.83 × 6.97 Å)[47] for RB are comparable to the host dimensions; hence, it is apparent that ZIF-7 can accommodate a guest Rhodamine-B within its pockets. The important reason for the selection of Rhodamine-B as a guest species lies in its interesting fragments and switch-on/switch-off states of fluorescence. However, an exact match between the pore metrics and the aromatic backbone of benzimidazole is advantageous for opting for ZIF-7 as a host material, as shown in Fig. 1. The encapsulation study was attempted using *in situ* encapsulation. Efforts to control the fluorescence states of guest species in the confined environment of ZIF-7 have resulted in an exciting series of host–guest compounds, accompanied by exciting fluorescence properties.

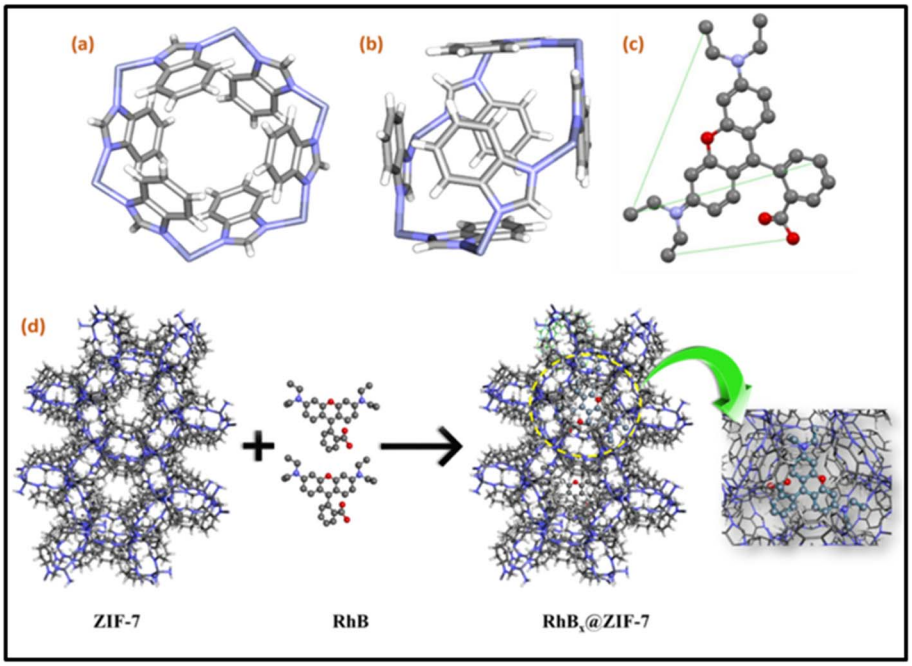

Fig. 1 Illustration of the ZIF-7 structure in two different orientations (a and b) and RhB with molecular dimensions (c). Schematic representation of RhB occupying pores of ZIF-7 (d).

2. Experimental

2.1. Instrumentation

The crystal structure of MOF and its composites was studied using a Powder X-ray diffractometer (Rigaku Mini Flex600 XRD, USA), with Cu Kα radiation at 25 °C. The optical studies were investigated using a UV spectrophotometer (Shimadzu UV-1800) and spectrofluorophotometer (Shimadzu RF-6000), which were recorded at room temperature. Functional group determination of the composites was performed using a Fourier transform infrared (FTIR) spectrometer (Shimadzu-A224056, Japan) and Raman microscopy (Renishaw Raman inVia Confocal microscope, UK). Scanning electron microscopy (APREO2, USA) was used for the surface morphology analysis. Thermal stability was investigated using a TGA/DTA Analyzer (NETZSCH, NJA – STA 2500 Regulus). Nitrogen adsorption studies were done using Gas Adsorption Analyzer (Microtrac, BELSORP-miniX, Japan). Lifetime studies were investigated using Sophisticated Fluorescence Spectrometer (EDINBURGH FLS 1000).

2.2. Chemicals and reagents

Zinc nitrate [($Zn(NO_3)_2 \cdot 6H_2O$), 98%], *N*,*N*′-dimethylformamide [DMF, 99%], acetone [($(CH_3)_2CO$, 99%], triethylamine [NEt_3, 98%], and Rhodamine-B [RhB] were purchased from Avra Synthesis Pvt. Ltd, Telangana, India. Benzimidazole [BIm, $C_7H_6N_2$] was purchased from Spectrochem Pvt., Ltd, Mumbai, India. Ultra-pure deionized water was collected from the Milli-Q (IQ 7000) ultrapure water purification system. All the chemicals were used as received without further purification.

2.3. Synthesis of pristine ZIF-7

0.75 mM $Zn(NO_3)_2 \cdot 6H_2O$ was dissolved in 5 mL of DMF taken in a 15 mL glass vial to obtain solution A. 1.87 mM BIm was dissolved in 5 mL of DMF taken in another 15 mL glass vial. Then, 1.87 mM NEt_3 was added and ultrasonicated to obtain solution B. Solutions A and B were mixed in a 50 mL conical flask and stirred well at 300 rpm for 30 min to obtain a white precipitate. The precipitate was washed with DMF and acetone three times, followed by drying at a temperature of 60 °C for 24 h to obtain white crystals.

2.4. *In situ* synthesis of RhB$_x$@ZIF-7

0.75 mM $Zn(NO_3)_2 \cdot 6H_2O$ was dissolved in 5 mL of DMF taken in a 15 mL glass vial to obtain solution A. 1.87 mM BIm was dissolved in 5 mL of DMF taken in another 15 mL glass vial. Then, 1.87 mM NEt_3 was added and ultrasonicated to obtain solution B. Solutions A and B were mixed in a 50 mL conical flask. Then, different amounts of RhB (10, 30, and 50 mg) were added to the conical flask and stirred at 250 rpm for 30 min, resulting in the formation of pink precipitates, RhB$_x$@ZIF-7 ($x = 10, 30, 50$). The products were washed several times with DMF and acetone until the pink colour disappeared from the supernatant solution. The pink precipitate was dried at 60 °C for 24 h to obtain the crystals for further use (Fig. 2).

3. Results and discussion

3.1. Characterization of ZIF-7 and RhB$_x$@ZIF-7

The Raman spectrum of pristine ZIF-7 (Fig. 3a) showed a sharp peak at 120 cm^{-1} associated with the lattice modes of vibration,

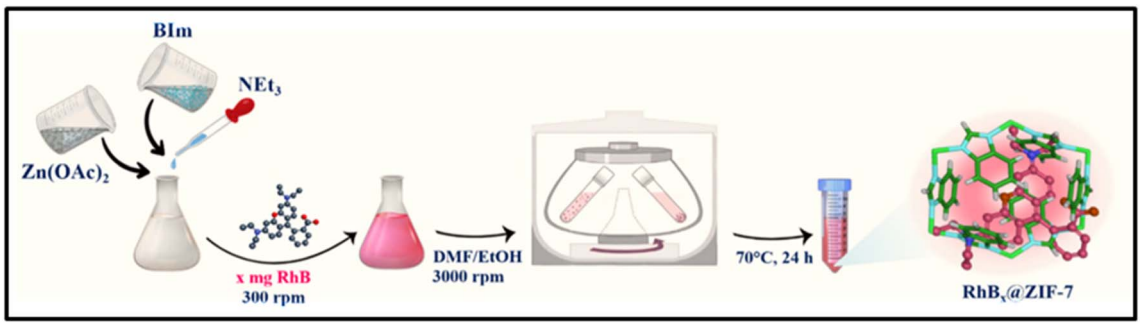

Fig. 2 Schematic of the synthesized RhB_x@ZIF-7.

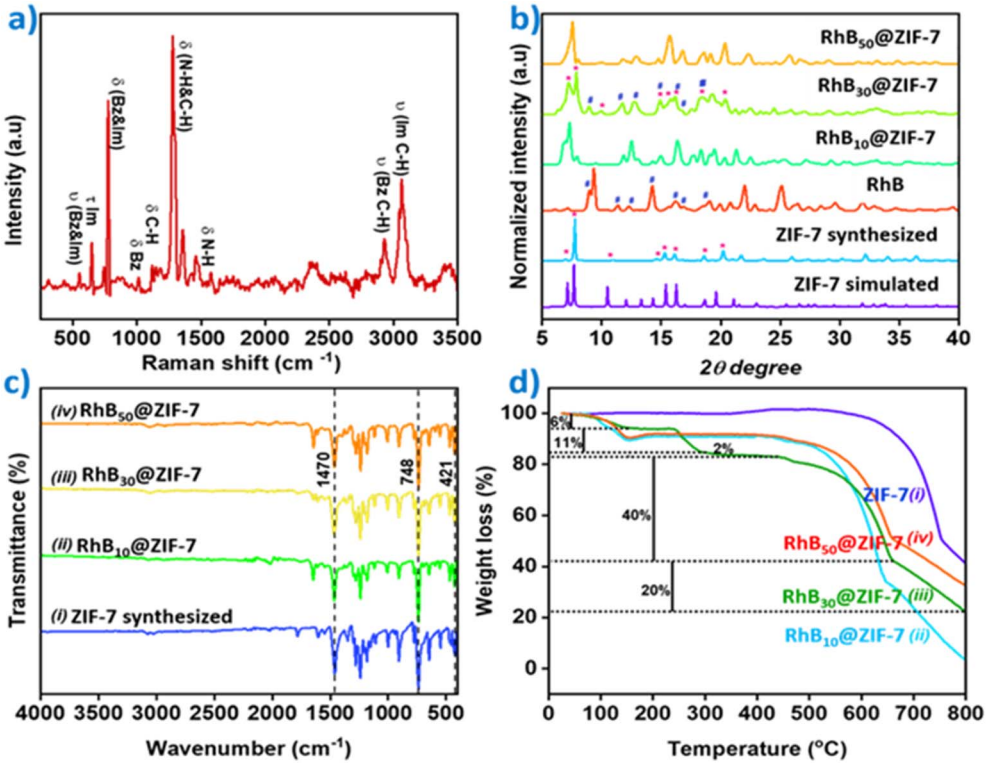

Fig. 3 (a) Raman spectrum of pristine ZIF-7. (b) The X-ray diffractogram showing the crystalline structure of simulated ZIF-7 [CCDC deposition number 602541], pristine ZIF-7, RhB [CCDC deposition number 1160674], RhB_{10}@ZIF-7, RhB_{30}@ZIF-7, and RhB_{50}@ZIF-7. (c) FT-IR spectra of (i) pristine ZIF-7, (ii) RhB_{10}@ZIF-7, (iii) RhB_{30}@ZIF-7 and (iv) RhB_{50}@ZIF-7. (d) TGA curves of (i) pristine ZIF-7, (ii) RhB_{10}@ZIF-7, (iii) RhB_{30}@ZIF-7 and (iv) RhB_{50}@ZIF-7.

along with the vibrational modes associated with the metal ligand interaction between zinc and benzimidazole nitrogen atoms. The peaks corresponding to bending modes of vibrations of the entire framework appeared at lower wavenumbers in the range of 200–800 cm^{-1}, and those corresponding to the vibrations of intra-framework bonds were found at 800–1600 cm^{-1} range, as expected.[58] A primary peak at 500 cm^{-1} was characteristic of the symmetric stretching of the imidazole ring in ZIF-7, along with the bending vibration mode of the imidazole ring at 645 cm^{-1}. The N–H and C–H vibrations of the imidazolate and benzene rings with π-conjugation and aromatic properties were supported by the peak at around 1590 cm^{-1}. A peak at 3000–3100 cm^{-1} showed aromatic C–H stretching vibrations of the benzene ring, while aliphatic C–H stretching vibrations were observed at around 2800–3000 cm^{-1}.[59]

The XRD pattern of as-synthesized RhB_x@ZIF-7 reveals the efficient inclusion of RhB into ZIF-7, retaining its crystallinity without framework disruption. The characteristic peaks of ZIF-7 match its simulated XRD pattern, as shown in Fig. 3b. The diffractogram revealed peaks at 2θ values 7.2°, 7.6°, 10.0°, 14.3°, 15.4°, 16.2°, 18.5°, and 20.4° assigned to the specific miller indices (101), (110), (021), (202), (220), (122), (113), and (140), respectively, confirming the crystallinity and purity of

synthesized pristine ZIF-7 (CCDC deposition no – 602541). The appearance of sharp peaks indicates its sodalite (SOD) topology and cubic crystal structure. The diffractogram of RhB_x@ZIF-7 retained characteristic peaks at 2θ values 7.2°, 7.8°, 10.0°, 14.9°, 15.7°, 16.2°, 18.5°, and 20.4°, indicating structural integrity of the framework. Distinct peaks of RhB were also visible at 2θ values of 9.2°, 11.3°, 12.8°, 14.6°, 16.1°, 16.7°, and 18.5°, corresponding to specific Miller indices (002), (020), (112), (022), (122), (113), and (004), respectively (CCDC deposition no – 1160674),[60] which confirmed the successful encapsulation of RhB into ZIF-7 with intact crystallinity. By introducing RhB into the pores of ZIF-7, the unit cell parameters are slightly disturbed, causing a change in the intensity and 2θ values in the XRD pattern.[47] Further, the typical patterns in the composite RhB_{30}@ZIF-7 are more in agreement with the aforementioned values.

Fig. 3c depicts the FTIR spectra of the synthesized pristine ZIF-7 and RhB_x@ZIF-7 composites analyzed in the range of 4000–300 cm^{-1} at room temperature. The stretching vibration of the C–N bond contributes to a characteristic sharp peak at 1640 cm^{-1}. All the samples give peaks at 1470 cm^{-1} and 748 cm^{-1}, corresponding to C–C and C–H vibrations in the benzimidazole ligand of ZIF-7, respectively. The peaks between 420 and 647 cm^{-1} represent the Zn–N bond in ZIF-7.[61] A decrease in the intensity of peaks between 600 cm^{-1} and 450 cm^{-1} corresponds to the non-covalent interaction between the hydroxyl group of RhB and the nitrogen of the imidazolate ring, and a similar characteristic peak of RhB was also observed in the same wavenumber between 600 cm^{-1} and 450 cm^{-1}.[52] The FTIR spectra of synthesized ZIF-7 and RhB_x@ZIF-7 composites showed a similar trend in peak positions, indicating structural similarity across all four samples. The obtained results suggest the encapsulation of RhB into ZIF-7 rather than adsorption onto its surface.

Thermogravimetric analysis (TGA) of pristine ZIF-7 and RhB_x@ZIF-7 composites showed weight loss due to non-coordinated and coordinated water molecules below 200 °C (*ca.* 6 wt%), as shown in Fig. 3d. Further weight loss observed below 300 °C indicates the decomposition of unreacted nitrates from the precursors and residual solvents trapped inside the framework (*ca.* 11 wt%).[62] The weight loss at temperatures in the range of 300–400 °C for RhB_x@ZIF-7 was attributed to the thermal degradation and destruction of encapsulated RhB (*ca.* 2 wt%).[57] The breakdown of the xanthene core of RhB leads to the formation of small organic fragments at 300 °C, and complete oxidation occurs at 400 °C, resulting in a carbonaceous residue. Among all the RhB_x@ZIF-7 (x = 10, 30, 50), the least solvent evaporation was observed in RhB_{30}@ZIF-7. The frameworks collapsed at temperatures above 500 °C, with a pronounced weight loss observed for all RhB_x@ZIF-7 samples and ZIF-7 (*ca.* 40 wt%).[34] Finally, a stable combustion product, ZnO, was obtained by complete degradation for all the samples.

In order to ensure the encapsulation of RhB molecules inside ZIF-7 pores rather than adsorbed onto its surface, controlled experiments were carried out. The synthesized RhB_x@ZIF-7 composites were immersed in doubly distilled deionized water, and RhB molecules were not released from the framework, giving a preliminary confirmation of RhB encapsulation into ZIF-7. To determine the content of loading RhB, the synthesized RhB_x@ZIF-7 composites were decomposed by acid hydrolysis, followed by UV spectrophotometer analysis. The loading fraction of RhB in ZIF-7 is determined as 0%, 0.069%, 2.0% and 8.4% for pristine ZIF-7, RhB_{10}@ZIF-7, RhB_{30}@ZIF-7, and RhB_{50}@ZIF-7, respectively (see Fig. S1 and Table S1). All these results demonstrate the loading of RhB into the ZIF-7 framework rather than adsorbed onto its surface.

In order to ensure the encapsulation of RhB molecules inside ZIF-7 pores rather than adsorbed onto its surface, controlled experiments were carried out. The synthesized RhB_x@ZIF-7 composites were immersed in doubly distilled deionized water, and RhB molecules were not released from the framework, giving a preliminary confirmation of RhB encapsulation into ZIF-7. To determine the content of loading RhB, the synthesized RhB_x@ZIF-7 composites were decomposed by acid hydrolysis, followed by UV spectrophotometer analysis. The loading fraction of RhB in ZIF-7 was determined as 0%, 0.069%, 2.0% and 8.4% for pristine ZIF-7, RhB_{10}@ZIF-7, RhB_{30}@ZIF-7, and RhB_{50}@ZIF-7, respectively (see Fig. S1 and Table S1). All these results demonstrate the loading of RhB into the ZIF-7 framework rather than adsorbed onto its surface.

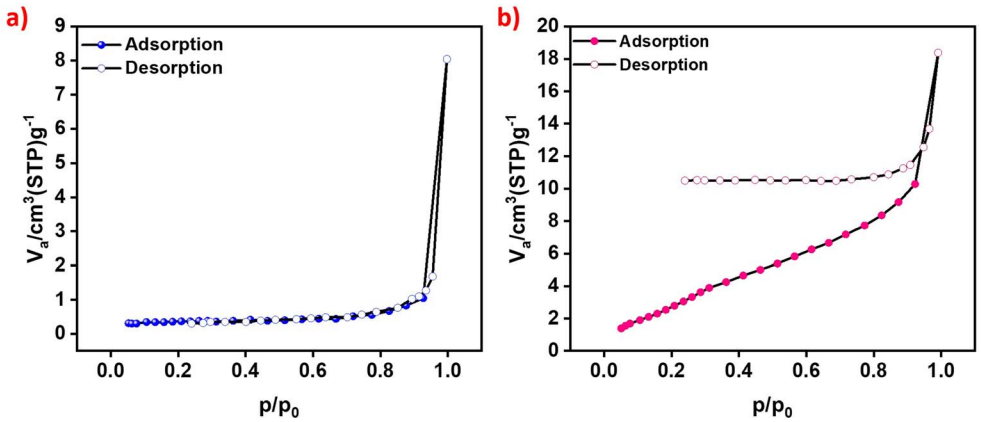

Fig. 4 N_2 adsorption–desorption isotherms of (a) pristine ZIF-7 and (b) RhB_{30}@ZIF-7.

The N_2 adsorption–desorption isotherms of pristine ZIF-7 and RhB_{30}@ZIF-7 were obtained at 77 K, as shown in Fig. 4. The BET surface area and pore volume measured for ZIF-7 are 1.27 $m^2\ g^{-1}$ and 0.011 $cm^3\ g^{-1}$, respectively (Fig. 4a). As suggested by previous reports, ZIF-7 is inaccessible to N_2 at 77 K because of the narrow pore openings compared to the kinetic diameter of N_2.[63] The sample clearly shows complete blockage of porosity up to a relative pressure of 0.8 with low adsorption capacity (0.61 mmol g^{-1}). Subsequently, an increase in the amount of N_2 intake was observed due to the condensation of the interparticle space.[64] For RhB_{30}@ZIF-7, the N_2 adsorption–desorption isotherms (Fig. 4b) exhibited a different shape over the evaluated relative pressure range. The nitrogen adsorption was irreversible, with an amount of N_2 trapped at a low relative pressure of 0.23. The BET surface area and pore volume are 13.9 $m^2\ g^{-1}$ and 0.028 $cm^3\ g^{-1}$, respectively. The increase in pore volume in RhB_{30}@ZIF-7 is due to the expansion of benzimidazole linkers connecting Zn metal clusters in the ZIF-7 framework to a porous structure when RhB was successfully encapsulated in its pores.[65]

The morphologies of the ZIF-7 and RhB_x@ZIF-7 and the effect of encapsulation were investigated using FE-SEM (Fig. 5) along with elemental mapping to understand RhB distribution over ZIF-7 (see Fig. S2–S5). The average particle size analysis is also determined using DLS analysis (see Fig. S6). The images confirm the cubic crystalline structure[63] of ZIF-7, as shown in Fig. 5a and b, with an average particle size distribution of 3.17 μm. RhB_{10}@ZIF-7 exhibited incomplete polyhedral structures of stacked nanosheet layers with stunted growth (Fig. 5c and d), with an average size distribution of 1.26 μm. Flower-like structures consisting of rod-shaped particles with non-uniform distribution indicate the defective crystal growth of ZIF-7 in RhB_{10}@ZIF-7. SEM images of RhB_{30}@ZIF-7 at different magnifications in Fig. 5e and f show a rhombic crystal structure,[66] with an average particle size distribution of 1.3 μm. Compared to ZIF-7, RhB_{30}@ZIF-7 had a smaller crystal size. This change in morphology was attributed to the effect of RhB encapsulation, which slows down the crystal growth of ZIF-7 at a rhombohedral shape with truncated corners before attaining the final rhombic dodecahedral shape.[9] Faceted structures with soft edges were observed in SEM micrographs of RhB_{50}@ZIF-7 (Fig. 5g and h). The particles exhibited a uniform size with an average particle size distribution of 1.61 μm. It was evident from the SEM images that as the concentration of RhB increased, the particle size also increased, among which RhB_{50}@ZIF-7 showed the highest particle size and RhB_{30}@ZIF-7 showed a well-defined polyhedral shape compared with other RhB_x@ZIF-7 composites. All these evidences confirm that the composite RhB_{30}@ZIF-7 has RhB encapsulated into ZIF-7 without any change in the crystal morphology, as expected for guest encapsulated ZIF-7. The incorporation of RhB_{30} into ZIF-7 enhances fluorescence due to its successful encapsulation into the pores of ZIF-7 compared to RhB_{10} and RhB_{50}. RhB in its solid state does not show emission due to aggregation-caused quenching (ACQ). However, when dispersed in a suitable medium (monomer separation), due to less aggregation, emission was enhanced. Although RhB was introduced to ZIF-7, it was either adsorbed onto the framework surface or encapsulated inside the MOF pores. Adsorbed dye molecules were easily lost or removed while dispersing the RhB_x@ZIF-7 composite in water or other media where RhB was soluble, leaving behind the RhB molecules occupied inside the MOF pores intact. As the concentration of RhB added to the MOF increases, the concentration of RhB occupying the ZIF-7 pores also increases, causing a disrupted framework.

The change in unit cell parameters/lattice parameters can be evident from the shape change from cubic to rhombic ZIF-7. The encapsulation of RhB into the pores decreases pore availability, making it a rhombic MOF composite. At most one RhB molecule can fit inside each pore of the framework due to the compatibility between the molecular size of RhB and the ZIF-7 pore structure. Such separation of RhB molecules helps to reduce ACQ, thereby enhancing luminescence efficiency. Even though the composite exists in a solid state, the encapsulated RhB gives fluorescence property to the RhB_x@ZIF-7 composite.

3.2. Optical properties of ZIF-7 and RhB_{30}@ZIF-7

UV-visible spectra of RhB, pristine ZIF-7, and RhBx@ZIF-7 are shown in Fig. S7a. Pristine ZIF-7 showed absorption maxima at 243 nm, 271 nm, and 277 nm, which aligns with the reported values below 300 nm (between 200 and 300 nm). UV-visible spectra of RhB show an absorption at a wavelength value of 554 nm.[60] The absorption maxima were shown at 242, 271, and

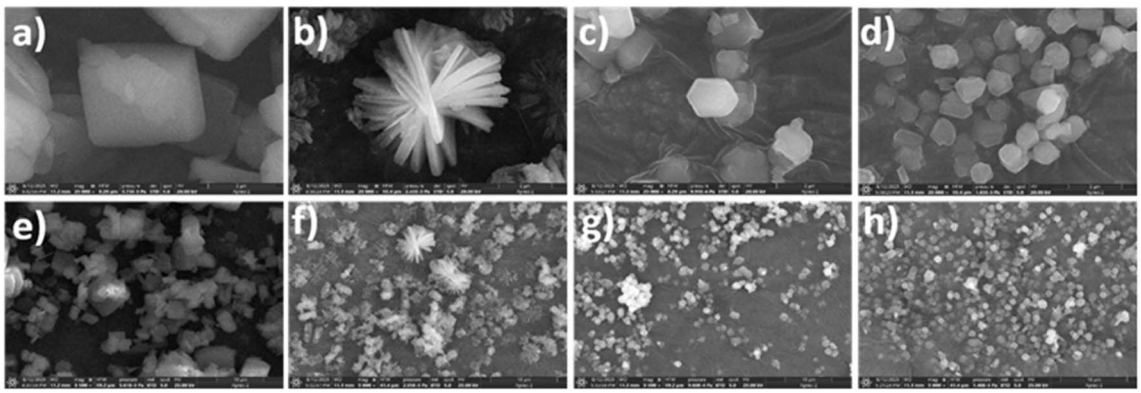

Fig. 5 FE-SEM images of (a and b) pristine ZIF-7, (c and d) RhB_{10}@ZIF-7, (e and f) RhB_{30}@ZIF-7, and (g and h) RhB_{50}@ZIF-7.

277 nm for RhB_{30}@ZIF-7. The presence of all the peaks corresponding to both the MOF and the absence of the absorption peak of the guest molecule, RhB, indicates successful encapsulation rather than adsorption.

The emission spectrum of ZIF-7 showed maximum intensity at 290 nm when excited at 271 nm, which was in agreement with the absorption spectra of ZIF-7 (Fig. S7b). There was no noticeable change in the emission wavelength of ZIF-7 when the excitation wavelength was changed. This type of behavior clearly depicts that the emission of ZIF-7 is independent of the excitation wavelength. The RhB_{30}@ZIF-7 shows dual emission at 290 nm and 578 nm, corresponding to both ZIF-7 and RhB, respectively, at $\lambda_{ex} = 271$ nm. At higher concentrations of RhB, the absorbance and emission were notable, whereas they were not at the lower concentrations of RhB in RhB_x@ZIF-7. This behavior in absorption and emission intensity suggests new insights into the maximum incorporation of guest molecules into the MOF pores, with a linear relation to the concentration of the guest molecule.

A comparison of the emission spectra at three different concentrations, 0.5, 1, and 2 mg mL^{-1} of ZIF-7, RhB_{10}@ZIF-7, RhB_{30}@ZIF-7, and RhB_{50}@ZIF-7 ($\lambda_{ex} = 271$ nm), respectively, is studied (Fig. S7c). A distinct trend in emission intensity was observed across the samples. The emission intensity increases at 0.5 and 1 mg mL^{-1} and decreases at 2 mg mL^{-1}, showing an irregular emission trend for ZIF-7, RhB_{10}@ZIF-7 and RhB_{50}@ZIF-7. In contrast, RhB_{30}@ZIF-7 showed a continuous increase in emission intensity from 0.5 mg mL^{-1} to 1 mg mL^{-1} and 2 mg mL^{-1}, with maximum intensity shown at 2 mg mL^{-1}. The mixed trend in the intensity of ZIF-7, RhB_{10}@ZIF-7, and RhB_{50}@ZIF-7 was due to the inner filter effect affecting the intensity of emission as the concentration increased. However, for RhB_{30}@ZIF-7, the inner filter effect was not observed, as the intensity showed a regular response with concentration increase.

4. Method development for the detection of melamine

The fluorescence response of RhB_{30}@ZIF-7 with the addition of melamine was evaluated in aqueous solutions. The emission intensity of RhB_{30}@ZIF-7 varies with parameters, such as pH, concentration of RhB_{30}@ZIF-7, incubation time, and temperature. The dual emissive system RhB_{30}@ZIF-7 showed emissions corresponding to both ZIF-7 and RhB at 290 nm and 578 nm, respectively, and both emissions were studied under different optimization parameters. The sensitivity and selectivity of the system towards melamine detection were enhanced by studying the effect of pH, concentration of RhB_{30}@ZIF-7, incubation time, and temperature.

4.1. Effect of pH

Melamine, as a weak base, has a pK_a value of 5.05, and the stability of RhB_{30}@ZIF-7 was affected by a change in pH. Therefore, the interaction between melamine and RhB_{30}@ZIF-7 was considerably affected by the pH of the sensing system. Further investigation on the effect of pH was performed by adjusting the pH of the solution, varying from 2.0 to 10.0, as shown in the SI (Fig. S8a). The PBS buffer, HCl, and NaOH were used to attain a specific pH for the desired reaction conditions. The 1 mg per mL RhB_{30}@ZIF-7 was added to each of the various pH solutions separately, along with the fixed concentration of melamine, and the emission spectra were recorded. The lowest intensity was observed at pH 7.0, while at pH levels less than 6.0 and above 8.0, the system showed high intensity due to framework rupture and release of RhB into the solution.

4.2. Effect of concentrations

To detect melamine, solutions of RhB_{30}@ZIF-7 with a range of concentrations (0.5 mg mL^{-1}, 1 mg mL^{-1}, and 2 mg mL^{-1}) were added to separate beakers; then, 100 μl of 1.0 M melamine solution was added to each of the beakers. In each case, a noticeable change in fluorescence intensity was observed. After 10 min of mixing melamine and RhB_{30}@ZIF-7, the emission intensity was studied (Fig. S8b). As the concentration of RhB_{30}@ZIF-7 increased from 0.5 mg mL^{-1} to 2.0 mg mL^{-1}, the detection efficiency was higher at 1.0 mg mL^{-1}. Therefore, 1 mg mL^{-1} of RhB_{30}@ZIF-7 was selected for further studies.

4.3. Effect of incubation time

During sensing studies, fluorescence measurements can be susceptible to incubation time after the addition of melamine into RhB_{30}@ZIF-7. The observations revealed that incubation time was crucial for melamine detection. The effect of incubation time in melamine detection was monitored, ranging from 0 to 20 min. 1 mg per mL RhB_{30}@ZIF-7 was added to 100 μl of 1.0 M melamine solution and kept for incubation while measuring the fluorescence intensity. The fluorescence intensity was measured at a specific time interval to identify the intensity variation over time. The emission intensity decreased steadily until it reached a lower maximum within 10 min. Then, emission intensity showed very little variation attributed to the maximum interaction between melamine and RhB_{30}@ZIF-7, as shown in the SI (Fig. S8c).

4.4. Effect of temperature

The hydrolysis of melamine can occur when the reaction conditions are changed. Therefore, the optimization of temperature in the detection of melamine is crucial. The effect of temperature was observed from 20 °C to 60 °C. 1 mg per mL RhB_{30}@ZIF-7 was added to 100 μl of 1.0 M melamine solution. The fluorescence quenching response was maximum at 30 °C (Fig. S8d) compared to other temperatures. Framework disruption and melamine hydrolysis to form cyanuric acid at high temperatures make it difficult to detect melamine at higher temperatures.

4.5. Performance of RhB_{30}@ZIF-7

100 mg of RhB_{30}@ZIF-7 was dispersed in 100 mL of Milli-Q water, and 100 μL of this solution was added to 1900 μL of doubly distilled ionized water and 1000 μL of PBS (pH 7.0)

buffer to achieve the final concentration of 33.3 μg mL^{-1}. The standard solutions of melamine with varying concentrations were added to the RhB_{30}@ZIF-7 solution. The fluorescence emission spectra were recorded at $\lambda_{ex} = 271$ nm after incubating the solution for 10 min at room temperature, as depicted in Fig. 6a. The selectivity of RhB_{30}@ZIF-7 towards melamine detection was further confirmed by the addition of possible interfering ions and chemicals in the presence of melamine.

4.6. Figures of merit

The limit of detection (LOD) and limit of quantification (LOQ) for the detection of melamine were determined using a plot of I_0/I *vs.* the concentration of melamine [M] (Fig. 6b). The LOD and LOQ were calculated using eqn (1) and (2), respectively. 'σ' is the standard deviation of the reaction at the minimum concentration, and 's' is the slope of the calibration curve.[27,28] The Stern–Volmer equation (eqn (3)) on the quenching effect was used to determine K_{sv}. I_o and I are the fluorescence intensities before and after the addition of melamine, and [M] is the molar concentration of melamine. The Stern–Volmer plot is shown in Fig. 6b. K_{sv} is the quenching effect coefficient of melamine.[29]

$$\text{Limit of detection (LOD)} = 3.3 \times (\sigma/s), \quad (1)$$

$$\text{Limit of quantification (LOQ)} = 10 \times (\sigma/s), \quad (2)$$

$$I_o/I = 1 + K_{sv}[M]. \quad (3)$$

Fig. 6b shows a linear relationship between I_0/I and [M], concentration of melamine in the range of 0–12 μM (0–1.51 ppm) and $R^2 = 0.99$, confirming the suitability of this method for sensing. Further, analysis of melamine shows an LOD of 0.47 μM (0.059 ppm) and an LOQ of 1.4 μM (0.1766 ppm), which are lower than the safety limits of melamine that should be present in adult food and infant formulations, *i.e.*, 2.5 ppm and 1 ppm, respectively. A comparison of the limit of detection achieved by various MOF composites for the optical sensing of melamine is shown in Table 1. Dual emissive MOF composite with dye encapsulation has not yet been explored, and the current work achieved an LOD value lower than the safety limit over a wide range of melamine concentrations.

4.7. Mechanism for the detection of melamine with RhB_{30}@ZIF-7

The fluorescence response of a dual emissive sensor based on RhB_{30}@ZIF-7 for melamine detection under optimized conditions was studied (Fig. 6c). The fluorescence emission intensity at $\lambda_{ex} = 271$ nm gradually decreased with an increase in the

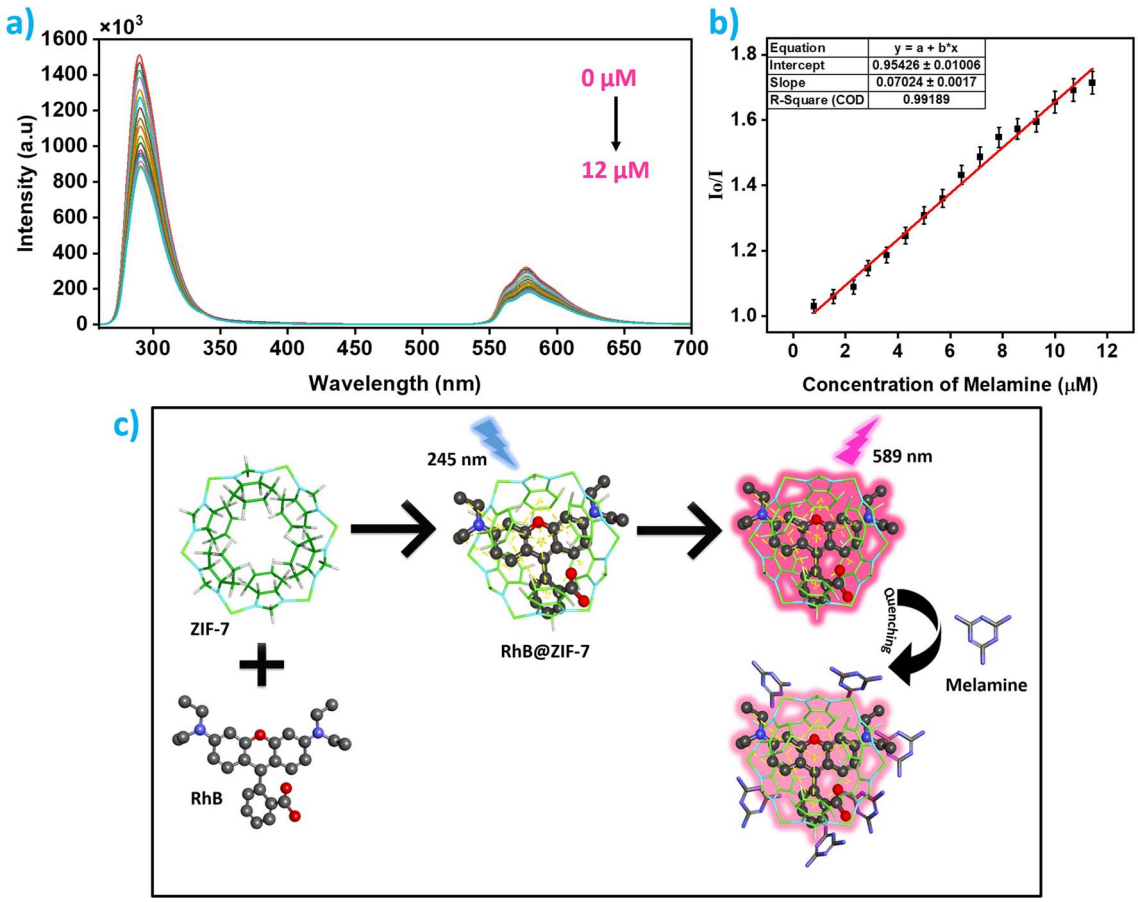

Fig. 6 (a) Fluorescence response of RhB_{30}@ZIF-7 with the addition of melamine. (b) SV plot showing the variation of fluorescence intensity of RhB_{30}@ZIF-7 with melamine concentration. (c) Schematic representation of fluorescence quenching on melamine addition.

Table 1 Comparison of the detection performance of various MOF composites for melamine detection

S. no	Material	Detection method	Tested matrix	Linear range	LOD (μM)	Ref.
1	Ag-MOF@Fe/SnO_2	Colorimetric detection	Raw milk	39.6–198.0 μM	14.27	27
2	UiO-66-NH_2@Ru	Fluorescent sensing	Milk powder	0.27–110 μM	90×10^{-3}	31
3	$CsPbBr_3$/HZIF-8	Fluorescent sensing	Raw milk Infant formulation	$3–500 \times 10^{-3}$ μM	2.64×10^{-3}	30
4	CeO_2@NH_2-MIL(Fe)	Fluorescent biosensing	Milk Milk powder Protein beverages	0–0.05 μM	7.6×10^{-3}	29
5	CeO_2-MIL(Fe)	Colorimetric detection	Milk Milk powder	0–0.1 μM	8.0×10^{-3}	28
6	RhB_{30}@ZIF-7	Fluorescent detection	Infant formulation	0–12 μM	0.47 μM	This work

melamine concentration. The emissions at 290 nm and 578 nm corresponding to ZIF-7 and RhB, respectively, showed a quenching in response due to the addition of melamine in the concentration range of 0–15 μM. The XRD pattern of the recovered RhB_{30}@ZIF-7-melamine complex shows no significant change, indicating a non-collapsed ZIF-7 skeleton after melamine sensing, which is supported by UV-visible absorption studies. Interestingly, the internal filtering effect (IFE) results in significant fluorescent quenching by the competitive absorption of excited energy between the melamine and RhB_{30}@ZIF-7, or in some cases, through the absorption of fluorescent emission of RhB_{30}@ZIF-7.

Here, the absorption of melamine was observed to be 240 nm, with a shoulder peak at 277 nm. The emission wavelength of RhB_{30}@ZIF-7 appeared at 290 nm at an excitation wavelength of 271 nm (Fig. S9). An overlap in the absorption spectra of melamine with the excitation wavelength of RhB_{30}@ZIF-7 was observed. The competitive absorption of the excitation wavelength of RhB_{30}@ZIF-7 by melamine reduced the fluorescent intensity in the emission spectra. When the concentration of melamine increased, more energy was absorbed, resulting in the lower emission intensity of the RhB_{30}@ZIF-7 system in the presence of melamine. The IFE depended on the spectral overlap between the melamine and RhB_{30}@ZIF-7. Additionally, the specific functional groups (–OH and $–NH_2$) on the fluorescence sensing system RhB_{30}@ZIF-7 can alter the emission characteristics due to non-covalent interactions with melamine, thereby quenching fluorescence intensity. Further comparison on the lifetime decay analysis of RhB_{30}@ZIF-7 in the presence and absence of melamine was carried out (Fig. 7). The lifetimes before the addition of melamine and after the addition are found to be 6.6 ns. The absence of a significant change in lifetime value for both samples also confirms the IFE as a sensing mechanism rather than any other mechanisms involving energy transfer between the sensing probe and the analyte.[67]

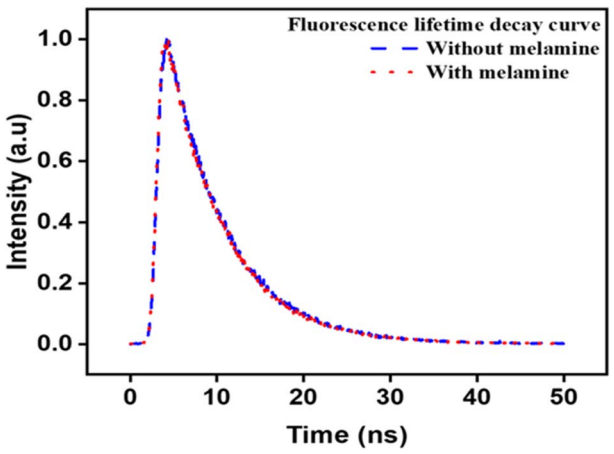

Fig. 7 Lifetime decay comparison of RhB_{30}@ZIF-7 in the absence and presence of melamine.

4.8. Selectivity of the sensor

Selectivity is a key feature of an optical sensor in real-time applications. Interference studies were conducted in the presence of different potential interfering ions, and chemicals present in infant formulations were taken to ensure selectivity towards melamine. In the presence of K^+, Na^+, Mg^{2+}, Zn^{2+}, Mn^{2+}, Fe^{2+}, Ca^{2+}, glucose, lactose, glycine, lysine, and glutamic acid, high selectivity was observed for melamine, indicating RhB_{30}@ZIF-7 as a potential dual emissive fluorescence sensing probe for melamine detection (Fig. S10).

5. Real sample analysis

5.1. Sample pre-treatment

2 g of infant formula powder was dissolved in 1.2 mL of CH_3-COOH and 1.5 mL of $CHCl_3$. The solution was stirred and centrifuged for about 20 min to obtain a homogeneous suspension. The supernatant solution was collected and diluted with 1000 mL of Milli-Q water, followed by centrifugation for 10 min at 3000 rpm while maintaining a pH of 7.0.

5.2. Analysis of unspiked and spiked samples

50 μl of 1 mg per mL RhB_{30}@ZIF-7, 2500 μl of pH 7.0 PBS, and 450 μl pre-treated infant formula solutions were added. This solution was kept for 10 min of incubation at room temperature, and the fluorescence spectra of each sample were analysed under the optimized conditions. Different concentrations of melamine solutions were added separately into pre-treated infant formula samples along with RhB_{30}@ZIF-7, and

Table 2 Determination of melamine in infant formula samples using the RhB_{30}@ZIF-7 fluorescent sensing platform

Real samples	Added (μM)	Found (μM)	% Recovery ($n = 5$)	RSD[a] (%)
Sample I[b]	0	ND	—	—
	1.0	1.01 ± 0.05	101.0	4.95
	2.0	2.13 ± 0.07	106.5	3.29
Sample I[c]	0	ND	—	—
	1.0	1.03 ± 0.04	103.0	3.88
	2.0	2.03 ± 0.07	101.5	3.45
Sample I[d]	0	ND	—	—
	1.0	0.99 ± 0.035	99.0	3.54
	2.0	2.04 ± 0.05	102.0	2.45
Sample I[e]	0	ND	—	—
	1.0	1.01 ± 0.035	101.0	3.47
	2.0	2.21 ± 0.07	110.5	3.17

[a] $n = 5$ individual determination % Recovery $= \frac{\text{found}}{\text{added}} \times 100$. [b] I: Amulspray, Gujarat Co-operative Milk Marketing Federation, Gujarat. [c] I: Lactogen Pro, Nestle India Limited, New Delhi. [d] I: Zerolac, Raptakos, Brett & Co. Ltd, Maharashtra. [e] I: Novel, British Life Sciences, Bangalore, Karnataka.

a similar procedure was followed to detect the concentration of melamine.

5.3. Detection of melamine in infant formulations

To confirm the accuracy of RhB_{30}@ZIF-7 for sensing melamine in infant formulations, the standard addition method was adopted. The pre-treatment of infant formulation samples was performed using the aforementioned method. The results indicated no detection of melamine in the unspiked infant formulation samples using the RhB_{30}@ZIF-7 sensor. The fluorescent detection exhibited a relative standard deviation (RSD%, $n = 5$) of spiked infant formulation samples with melamine between 2.45% and 4.95%, and the recovery percentage was obtained between 99.00% and 106.5%, indicating the accuracy of the method, which suggests reliable precision and reproducibility, as shown in Table 2. The RSD values below 5% and the signal to noise ratio (SNR) analysis with an estimated SNR of 7 at 1 μM melamine, and the corresponding increase with concentration, highlight the high repeatability and sensitive detection even at very low concentrations. The SNR is greater than 70 at 10 μM, and its value across the evaluated concentration range indicates the stable signals obtained from the sensor with negligible background noise, thereby supporting the accuracy of the established linearity. All these results confirm the efficiency of RhB_{30}@ZIF-7 as a sensitive probe for melamine detection in a real sample matrix.

6. Conclusion

A novel fluorescent sensing probe, RhB_{30}@ZIF-7, was synthesized using a one-pot solvothermal method *via in situ* encapsulation of RhB into ZIF-7 pores. The resulting RhB_{30}@ZIF-7 fluorescent system has dual emissions due to the two components, ZIF-7 and RhB, present in it, enabling the fluorescent detection of melamine in real infant formula samples. The fluorescent intensity decreased at 290 nm and 578 nm upon the addition of melamine. The sensing system RhB_{30}@ZIF-7 showed a linear range between the concentration of melamine in the range of 0–12 μM, the LOD of melamine is evaluated to be 0.47 μM, and the LOQ of melamine is evaluated to be 1.4 μM, with an R^2 of 0.99. RhB_{30}@ZIF-7 can be used for the detection of melamine in real infant formula samples with good recovery (99.75–101.5%) and RSD (2.50–4.95%) values. Although the present study establishes the feasibility of dye-encapsulated fluorescein probe RhB_{30}@ZIF-7 for the ultrasensitive detection of melamine, future works could focus on broadening the applicability of the probe towards selective detection of other nitrogen-rich adulterants in complex food matrices.

Author contributions

Sreevidhya K. B.: investigation, formal analysis, methodology, writing – original draft and Suvardhan Kanchi: conceptualization, project administration, writing – review & editing.

Conflicts of interest

The authors declare that they have no known competing financial interests or personal relationships that could have appeared to influence the work reported in this paper.

Data availability

The data supporting this article have been included as part of the SI. Supplementary information: methods, SEM images, DLS particle size analysis, spectrophotometric and spectrofluorometric analysis. See DOI: https://doi.org/10.1039/d5na00633c.

Acknowledgements

The authors greatly acknowledge the funding provided by the Centre for Research, CHRIST University, in the form of seed funding with Ref. No. CU-ORS-SM-24/70. We sincerely thank Dr Abhijeet K Chaudhari for his valuable suggestions in synthesising the nanomaterials and their characterization.

References

1 J. R. Ingelfinger, *N. Engl. J. Med.*, 2008, **359**, 2745–2748.
2 R. A. Lynch, H. Hollen, D. L. Johnson and J. Bartels, *Int. J. Food Contam.*, 2015, **2**, 9.
3 M. F. Neerman, W. Zhang, A. R. Parrish and E. E. Simanek, *Int. J. Pharm.*, 2004, **281**, 129–132.
4 P. Goyal, P. Soppina, S. K. Misra, E. Valsami-Jones, V. Soppina and S. Chakraborty, *Front. Toxicol.*, 2022, **4**, 917749.
5 Y. C. Tyan, M. H. Yang, S. B. Jong, C. K. Wang and J. Shiea, *Anal. Bioanal. Chem.*, 2009, **395**, 729–735.
6 S. Öztürk and N. Demir, *J. Food Compos. Anal.*, 2021, **100**, 103931.
7 W. Chansuvarn, S. Panich and A. Imyim, *Spectrochim. Acta, Part A*, 2013, **113**, 154–158.
8 M. M. Deabes and R. El-Habib, *J. Environ. Anal. Toxicol.*, 2012, **02**, 4.

9 E. W. P. Moore and F. Maya, *Nanomaterials*, 2023, **13**, 842.
10 H. Sun, L. Wang, L. Ai, S. Liang and H. Wu, *Food Control*, 2010, **21**, 686–691.
11 M. S. Filigenzi, B. Puschner, L. S. Aston and R. H. Poppenga, *J. Agric. Food Chem.*, 2008, **56**, 7593–7599.
12 R. A. Yokley, L. C. Mayer, R. Rezaaiyan, M. E. Manuli and M. W. Cheung, *J. Agric. Food Chem.*, 2000, **48**, 3352–3358.
13 J. P. Toth and P. C. Bardalaye, *J. Chromatogr.*, 1987, **408**, 335–340.
14 Y. Wen, H. Liu, P. Han, Y. Gao, F. Luan and X. Li, *J. Sci. Food Agric.*, 2010, **90**, 2178–2182.
15 W. Yin, J. Liu, T. Zhang, W. Li, W. Liu, M. Meng, F. He, Y. Wan, C. Feng, S. Wang, X. Lu and R. Xi, *J. Agric. Food Chem.*, 2010, **58**, 8152–8157.
16 F. Sun, L. Liu, H. Kuang and C. Xu, *Food Agric. Immunol.*, 2013, **24**, 79–86.
17 E. Koglin, B. J. Kip and R. J. Meier, *J. Phys. Chem.*, 1996, **100**, 5078–5089.
18 Z. Guo, Y.-t. Zhao, Y.-h. Li, T. Bao, T.-s. Sun, D.-d. Li, X.-k. Luo and H.-t. Fan, *Food Anal. Methods*, 2017, **11**, 546–555.
19 J. An, L. Li, Y. Ding, W. Hu, D. Duan, H. Lu, D. Ye, X. Zhu and H. Chen, *Electrochim. Acta*, 2019, **326**, 134946.
20 M. Alizadeh Sani, G. Jahed-Khaniki, A. Ehsani, N. Shariatifar, M. H. Dehghani, M. Hashemi, H. Hosseini, M. Abdollahi, S. Hassani, Z. Bayrami and D. J. McClements, *Biosensors*, 2023, **13**, 94.
21 M. Angelopoulou, P. Petrou and S. Kakabakos, *TrAC, Trends Anal. Chem.*, 2024, **175**, 117714.
22 S. Oliveira, M. Sharifuzzaman, G. Moro, A. Sinibaldi, Z. Altintas, S. Kumar, F. Chiavaioli and C. Marques, *TrAC, Trends Anal. Chem.*, 2025, **184**, 118139.
23 Z. Ling, L. Yang, W. Zhang, T. Yao and H. Xu, *Food Saf. Health*, 2024, **2**, 72–95.
24 M. Shellaiah and K. W. Sun, *Chemosensors*, 2019, **7**, 9.
25 Q. Xu, F. Xiao and H. Xu, *Trends Anal. Chem.*, 2023, **161**, 116999.
26 Y. Zhao, H. Zeng, X. W. Zhu, W. Lu and D. Li, *Chem. Soc. Rev.*, 2021, **50**, 4484–4513.
27 T. Shahzadi, H. Bibi, T. Riaz, M. Zaib and T. Malik, *Plasmonics*, 2025, **20**, 1169–1181.
28 A. Amalraj, M. Narayanan and P. Perumal, *Analyst*, 2022, **147**, 3234–3247.
29 A. Amalraj and P. Perumal, *New J. Chem.*, 2022, **46**, 12952–12967.
30 S. Ahmed, S. Lahkar, S. Doley, D. Mohanta and S. Kumar Dolui, *J. Photochem. Photobiol., A*, 2023, **443**, 114821.
31 C. Lin, C. Zhong, Y. Song and L. Wang, *Microchem. J.*, 2021, **162**, 105837.
32 S. R. Venna and M. A. Carreon, *J. Am. Chem. Soc.*, 2010, **132**, 76–78.
33 K. S. Park, Z. Ni, A. P. Cote, J. Y. Choi, R. Huang, F. J. Uribe-Romo, H. K. Chae, M. O'Keeffe and O. M. Yaghi, *Proc. Natl. Acad. Sci. U. S. A.*, 2006, **103**, 10186–10191.
34 X. C. Huang, Y. Y. Lin, J. P. Zhang and X. M. Chen, *Angew Chem. Int. Ed. Engl.*, 2006, **45**, 1557–1559.
35 Y. Zhu, X. Sun, Y. Tang, L. Fu and Y. Lu, *Nano Res.*, 2020, **14**, 1912–1936.
36 X. Huang, J. Zhang and X. Chen, *Chin. Sci. Bull.*, 2003, **48**, 1531–1534.
37 M. J. Dong, M. Zhao, S. Ou, C. Zou and C. D. Wu, *Angew Chem. Int. Ed. Engl.*, 2014, **53**, 1575–1579.
38 H.-R. Fu, L.-B. Yan, N.-T. Wu, L.-F. Ma and S.-Q. Zang, *J. Mater. Chem. A*, 2018, **6**, 9183–9191.
39 S.-J. Qin and B. Yan, *Sens. Actuators, B*, 2018, **272**, 510–517.
40 J. Yoo, U. Ryu, W. Kwon and K. M. Choi, *Sens. Actuators, B*, 2019, **283**, 426–433.
41 H. Zhao, J. Ni, J. J. Zhang, S. Q. Liu, Y. J. Sun, H. Zhou, Y. Q. Li and C. Y. Duan, *Chem. Sci.*, 2018, **9**, 2918–2926.
42 J. Wang, Y. Zhang, Y. Yu, F. Ye, Z. Feng, Z. Huang, X. Liu and X. Zhou, *Opt. Mater.*, 2019, **89**, 209–213.
43 Y. Tang, W. He, Y. Lu, J. Fielden, X. Xiang and D. Yan, *J. Phys. Chem. C*, 2014, **118**, 25365–25373.
44 Z. Sun, A. Khurshid, M. Sohail, W. Qiu, D. Cao and S. J. Su, *Nanomaterials*, 2021, **11**, 2761.
45 M. J. Snare, F. E. Treloar, K. P. Ghiggino and P. J. Thistlethwaite, *J. Photochem.*, 1982, **18**, 335–346.
46 R. Sjöback, J. Nygren and M. Kubista, *Spectrochim. Acta, Part A*, 1995, **51**, L7–L21.
47 Y. Zhang, M. Gutierrez, A. K. Chaudhari and J. C. Tan, *ACS Appl. Mater. Interfaces*, 2020, **12**, 37477–37488.
48 A. K. Chaudhari and J. C. Tan, *Adv. Opt. Mater.*, 2020, **8**, 1901912.
49 R. Xu, Y. Wang, X. Duan, K. Lu, D. Micheroni, A. Hu and W. Lin, *J. Am. Chem. Soc.*, 2016, **138**, 2158–2161.
50 C. He, K. Lu and W. Lin, *J. Am. Chem. Soc.*, 2014, **136**, 12253–12256.
51 M. Gutierrez, Y. Zhang and J. C. Tan, *Chem. Rev.*, 2022, **122**, 10438–10483.
52 Y. Zhang and J. C. Tan, *iScience*, 2021, **24**, 103035.
53 L. Yang, Y. L. Liu, C. G. Liu, Y. Fu and F. Ye, *RSC Adv.*, 2020, **10**, 19149–19156.
54 J. Hassanzadeh, H. A. J. Al Lawati and I. Al Lawati, *Anal. Chem.*, 2019, **91**, 10631–10639.
55 D. A. Sherman, M. Gutiérrez, I. Griffiths, S. Mollick, N. Amin, A. Douhal and J. C. Tan, *Adv. Funct. Mater.*, 2023, **33**, 2214307.
56 J. P. Zheng, S. Ou, M. Zhao and C. D. Wu, *Chempluschem*, 2016, **81**, 758–763.
57 Y. Gao, Y. Qi, K. Zhao, Q. Wen, J. Shen, L. Qiu and W. Mou, *Sens. Actuators, B*, 2018, **257**, 553–560.
58 K. Kamali, S. Prasad, M. K. Sahoo, J. N. Behera, U. V. Waghmare and C. Narayana, *Inorg. Chem.*, 2022, **61**, 11571–11580.
59 K. Kamali, B. Joseph and C. Narayana, *J. Solid State Chem.*, 2022, **309**, 122973.
60 X. Wang, M. Song and Y. Long, *J. Solid State Chem.*, 2001, **156**, 325–330.
61 A. Davoodi, K. Akhbari and M. Alirezvani, *CrystEngComm*, 2023, **25**, 3931–3942.
62 K. Kim, K. J. Lopez, H.-J. Sun, J.-C. An, G. Park and J. Shim, *J. Appl. Electrochem.*, 2018, **48**, 1231–1241.
63 A. Arami-Niya, G. Birkett, Z. Zhu and T. E. Rufford, *J. Mater. Chem. A*, 2017, **5**, 21389–21399.

64 C. Cuadrado-Collados, J. Fernández-Català, F. Fauth, Y. Q. Cheng, L. L. Daemen, A. J. Ramirez-Cuesta and J. Silvestre-Albero, *J. Mater. Chem. A*, 2017, **5**, 20938–20946.
65 Y. Du, B. Wooler, M. Nines, P. Kortunov, C. S. Paur, J. Zengel, S. C. Weston and P. I. Ravikovitch, *J. Am. Chem. Soc.*, 2015, **137**, 13603–13611.
66 M. Gustafsson and X. Zou, *J. Porous Mater.*, 2013, **20**, 55–63.
67 S. Kumar Panigrahi and A. Kumar Mishra, *J. Photochem. Photobiol., C*, 2019, **41**, 100318.